Optics Communications 456 (2020) 124549

Contents lists available at ScienceDirect

Optics Communications

journal homepage: www.elsevier.com/locate/optcom

Impact of random segment pose errors for deployable telescope and its tolerance allocation

Huisheng Yang [a,b,*], Xuejun Zhang [a], Zhilai Li [a], He Bao [a]

[a] Changchun Institute of Optics, Fine Mechanics and Physics, Chinese Academy of Sciences, Changchun 130033, China
[b] University of Chinese Academy of Sciences, Beijing 100049, China

ARTICLE INFO

Keywords:
Ultra large aperture
Space-based telescope
Segmented primary mirror
Pose errors
Wavefront deformation

ABSTRACT

Segmented primary mirror is very sensitive to co-phasing errors, especially the random segment pose errors produced by positioning deviations. This paper proposes the linear sensitivity matrix of the pose-error-caused wavefront deformation, derives the corrected-prediction formula of the deformation, and presents a method of weighted tolerance allocation in order to control the pose-phasing platform cost. Results indicate that random pose errors will generate uncertain wavefront deformation, which can be predicted by the formula with prediction errors of the expectation less than ±1% and variance less than ±5%. And the technical difficulty of the platform construction can be minimized using the allocation method.

1. Introduction

Scientists desire larger-aperture telescopes to obtain greater light-gather power and spatial resolution, which are the prerequisite for exploring and researching the earth-like planets [1,2]. Study from National Aeronautics and Space Administration (NASA) shows that the discovery speed of earth-like planets is directly proportional to the 1.8th power of the aperture D and the 0.4th power of the time t, thus a telescope with aperture larger than 8 m is necessary to meet the basic requirements of astronomy observation [3,4]. In order to achieve this target, nearly a dozen 8 m to 10 m telescopes are currently in operation on the ground, and telescopes with apertures 30, 50, and even 100 meters in diameter are under development [5]. However, because of the effects of earth atmosphere and diurnal thermal cycling, ground-based telescope cannot achieve diffraction-limited imaging. For addressing this problem, the space-based telescope with ultra-large-aperture is imperative.

Due to the limitation of the launch fairing, space-based telescope with aperture larger than 4 m should adopt the segmented and deployable primary mirror (PM) [6,7], which means the telescope must be folded before launch and deployed or assembled on orbit. For examples, the James Webb Space Telescope (JWST) with aperture 6.5 m in diameter [8], the Advanced Technology Large Aperture Space Telescope (ATLAST) with aperture larger than 8 m [9] and the Thirty Meter Space Telescope (TMST) [10] are all segmented telescopes. One of the most critical techniques for deployable telescopes is the segmented PM co-phasing, which include two aspects: one is to make segments possess correct aspheric parameters (surface-shape phasing), and the other is to accurately calibrate the segments' position and attitude (pose phasing). When properly phased relative to each other, the segmented telescope can achieve the imaging capability equivalent to design aperture, otherwise only equivalent to the aperture of one segment [11].

Segment pose phasing is a challenging task, which requires the phasing mechanism within sub-millimeter travel must be able to possess nanometer accuracy. This indicator is tremendously difficult to achieve because of the numerous limitations from the space environment. To address this problem, the impact of segment pose errors should be thoroughly studied, and the pose tolerances must be properly allocated in order to reduce the demand for pose-phasing precision. At present, the research on co-phasing errors mainly focuses on the error detection [12–15] and the influences of piston and tip/tilt errors with definite value and defined in PM coordinate system [16–22]. The analysis of impacts of segment random pose errors originating from co-phasing platform insufficient precision is rarely concerned. This is because it involves many disciplines, and the randomness of pose error can also bring significant research difficulties. However, this analysis is necessary and significant especially in high-precision imaging systems, which can resolve that whether the pose-phasing tolerance allocation is reasonable, and how to reduce the development cost and difficulties of the segmented PM co-phasing system.

This paper proposes a method of weighted tolerance allocation to control the cost of segment pose-phasing platform. Firstly, it introduces the basic composition of a segmented PM and analyzes the sources of segments pose errors. The linear sensitivity matrix of the wavefront deformation (WD) to segments pose errors defined in local coordinate system (LCS) is then derived, the prediction formula of the WD

* Corresponding author at: Changchun Institute of Optics, Fine Mechanics and Physics, Chinese Academy of Sciences, Changchun 130033, China.
E-mail address: yanghuisheng@126.com (H. Yang).

https://doi.org/10.1016/j.optcom.2019.124549
Received 22 June 2019; Received in revised form 11 August 2019; Accepted 8 September 2019
Available online 13 September 2019

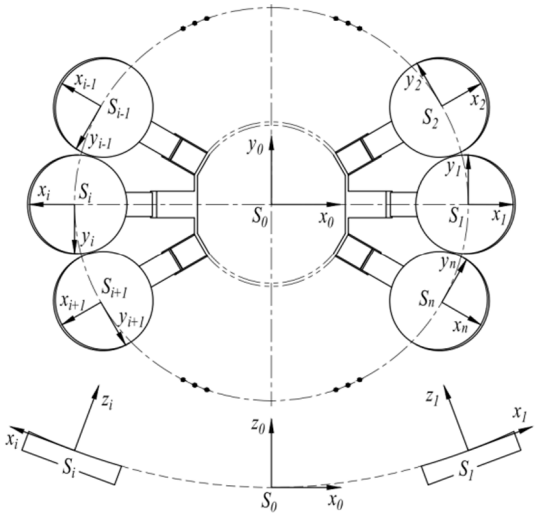

Fig. 1. Segmented primary mirror.

stemming from segments random pose errors is deduced, and Monte Carlo simulations are achieved to verify the validity of the prediction. Finally, we present the method of weighted tolerance allocation, and demonstrate the actual effect using numerical simulations.

2. Segmented primary mirror architecture and sources of segments pose errors

Fig. 1 illustrates a segmented PM composed of 10 mirror segments, which is a PM configuration scheme for a deployable optical system (described in Ref. [23]) in a funded project by the Ministry of Science and Technology of China. This project comes from the "National Key Research and Development Program of china" – Geostationary Orbit High Resolution Light Imaging Camera System Technology (Grant No. 2016YFB0500100), and is aimed to study the implementation and related basic technologies of ultra-large-aperture telescopes. Each segment has the same prescription: 1.9 m in diameter, paraxial radius of curvature (ROC) 10 m and conic constant −1. When properly phased relative to each other, these segments act as a single mirror which can provide an 8 m aperture for the observatory. $\{S_0\}$ is the global coordinate system (GLS) and locates at the vertex of PM nominal surface, the z-axis of which coincides with the principle axis, the x-axis is along the $\overline{S_0S_i}$ projection on the paper surface. There are m LCSs. $\{S_i\}$ is the LCS corresponding to the segment S_i, its z-axis coincides with the segment structural axis, origin coincides with the intersection of the z-axis and segment surface, x-axis is in the plane $S_0S_iz_i$ and perpendicular to the z-axis, and y-axis is determined by right-hand rule.

Most PM used in high precision optical systems have nominal conic-section-of-revolution surface shape. A co-phasing platform with at least five DOFs is the prerequisite for the phase alignment of segments with this surface shape. Because of the advantages of compact structure, little space occupation, high structural stiffness, large carrying capacity, few error accumulation and high precision, parallel mechanism has been the first choice for the co-phasing platform. Fig. 2 shows a typical six DOF parallel platform, which mainly consists of fixed platform, moving platform and six linear actuators. The segment is mounted to the moving platform. Therefore, the segment pose errors are equivalent to the platform positioning errors. Sources of platform positioning errors mainly include fit clearance, creeping phenomenon and control errors, which will result in that the moving platform stops at undetermined position and with undetermined attitude. This randomness of positioning errors will lead to slight perturbations in the other five DOF, even though the platform just moves along one DOF. According

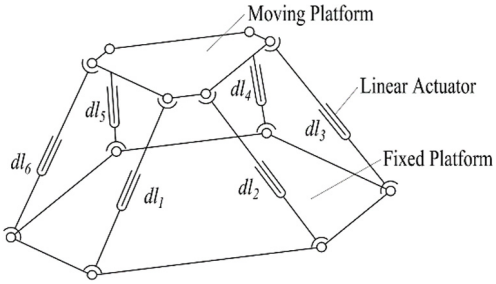

Fig. 2. Diagram of a pose-phasing platform with six DOFs rigid body motions.

to practical experience, the positioning errors approximatively follow multidimensional independent uniform distribution [24,25]:

$$\Delta X_i \sim \mathrm{U}[a_i, b_i] \tag{1}$$

where $\Delta\mathbf{X} = [\Delta\theta_x, \Delta\theta_y, \Delta\theta_z, \Delta\delta_x, \Delta\delta_y, \Delta\delta_z]^T$ is a vector composed of segment pose error ΔX_i. $\Delta\theta$ is attitude error. $\Delta\delta$ is position error. a_i and b_i are the error bounds of ΔX_i.

The expectation and variance of ΔX_i can be written as:

$$E\Delta X_i = \frac{a_i + b_i}{2} = 0\ ; \quad D\Delta X_i = \frac{(b_i - a_i)^2}{12} = \sigma_i^2 \tag{2}$$

3. Wavefront deformation originating from segment pose errors

3.1. Basic theory

According to geometric ray-trace optics, an incident-ray stemming from the nominal wavefront and reflected by segment can be expressed by the functions of the surface-shape, the segment position and attitude, as well as the position and direction of the incident-ray:

$$\begin{aligned} \hat{\mathbf{r}} &= f(R, k, \boldsymbol{\delta}, \boldsymbol{\theta}, \hat{\boldsymbol{i}}, \boldsymbol{p}) \\ \boldsymbol{\gamma} &= g(R, k, \boldsymbol{\delta}, \boldsymbol{\theta}, \hat{\boldsymbol{i}}, \boldsymbol{p}) \\ L &= h(R, k, \boldsymbol{\delta}, \boldsymbol{\theta}, \hat{\boldsymbol{i}}, \boldsymbol{p}) \end{aligned} \tag{3}$$

where R is the paraxial ROC. k is the conic constant. $\boldsymbol{\delta}$ is the segment position vector. $\boldsymbol{\theta}$ is the segment attitude vector. $\hat{\boldsymbol{i}}$ is the unit direction vector of the incident-ray. p is the position vector of the incident-ray. $\hat{\boldsymbol{r}}$ is the unit direction vector of the reflected-ray. $\boldsymbol{\gamma}$ is the reflected-ray transverse aberration (beamwalk) from the nominal ray position. L is optical path-length. $f(x)$, $g(x)$ and $h(x)$ are beam transfer functions.

Performing the Taylor series expansion for Eq. (3) and ignoring the higher order infinitesimal, the WD produced by the incident-ray perturbations $\Delta\hat{\boldsymbol{i}}$ and $\Delta\boldsymbol{a}$, as well as the segment pose perturbations $\Delta\boldsymbol{\delta}$ and $\Delta\boldsymbol{\theta}$ can be written as:

$$\begin{aligned} \Delta\hat{\boldsymbol{r}} &= \frac{\partial\hat{\boldsymbol{r}}}{\partial\hat{\boldsymbol{i}}}\cdot\Delta\hat{\boldsymbol{i}} + \frac{\partial\hat{\boldsymbol{r}}}{\partial\boldsymbol{p}}\cdot\boldsymbol{a}\frac{\partial\hat{\boldsymbol{r}}}{\partial\boldsymbol{\theta}}\cdot\Delta\boldsymbol{\theta} + \frac{\partial\hat{\boldsymbol{r}}}{\partial\boldsymbol{\delta}}\cdot\Delta\boldsymbol{\delta} \\ \Delta\boldsymbol{\gamma} &= \frac{\partial\boldsymbol{\gamma}}{\partial\hat{\boldsymbol{i}}}\cdot\Delta\hat{\boldsymbol{i}} + \frac{\partial\boldsymbol{\gamma}}{\partial\boldsymbol{p}}\cdot\boldsymbol{a}\frac{\partial\boldsymbol{\gamma}}{\partial\boldsymbol{\theta}}\cdot\Delta\boldsymbol{\theta} + \frac{\partial\boldsymbol{\gamma}}{\partial\boldsymbol{\delta}}\cdot\Delta\boldsymbol{\delta} \\ \Delta L &= \frac{\partial L}{\partial\hat{\boldsymbol{i}}}\cdot\Delta\hat{\boldsymbol{i}} + \frac{\partial L}{\partial\boldsymbol{p}}\cdot\boldsymbol{a}\frac{\partial L}{\partial\boldsymbol{\theta}}\cdot\Delta\boldsymbol{\theta} + \frac{\partial L}{\partial\boldsymbol{\delta}}\cdot\Delta\boldsymbol{\delta} \end{aligned} \tag{4}$$

where a is incident-ray transverse perturbation measured at the incident ray reference point.

Eq. (4) shows that segments pose errors can change reflected-rays direction, produce reflected-rays beamwalk and lead to the optical path difference (OPD). According to Ref. [26], the OPD originating from the incident-ray perturbations is zero. For an ultra-large aperture optical system, the PM is the first optical element through which incident-rays pass, so the incident wavefront is ideal and the incident-rays does not have perturbations. Therefore, the impact of segments pose errors can be expressed as:

$$\Delta OPT_{jk} = \frac{\partial L_k}{\partial\boldsymbol{\theta}}\Delta\boldsymbol{\theta}_j + \frac{\partial L_k}{\partial\boldsymbol{\delta}}\Delta\boldsymbol{\delta}_j \qquad \begin{matrix} 1 \le k \le n \\ 1 \le j \le m \end{matrix} \tag{5}$$

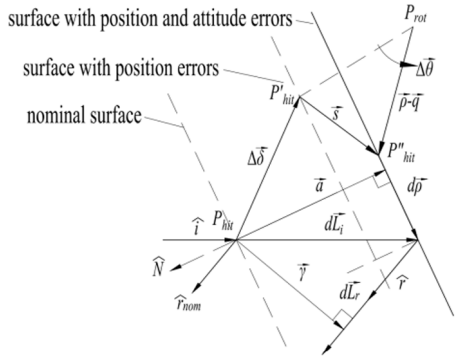

Fig. 3. An incident-ray is reflected by the segment with pose errors.

where ΔOPT_{jk} is the OPD of incident-ray k reflected by segment S_j. m is the quantity of all segments. n is the quantity of all incident-rays passing through segment S_j. $\Delta\boldsymbol{\theta}_j$ and $\Delta\mathbf{s}_j$ are attitude errors and position errors of segment S_j respectively.

Redding developed a series of coordinate-free ray-trace formulations, which can be used to produce the sensitivity matrix of the individual exit-pupil-ray OPD to the mirror pose errors defined in PM coordinate system [26]. The segment pose alignment is implemented in segment coordinate system, and the segment pose errors are also defined in LCS. Therefore, the sensitivity matrix of WD originating from the segment pose errors defined in LCS should be derived.

According to small-angle approximation, an incident-ray reflected by the segment with pose perturbations can be described by Fig. 3. The segment is firstly translated $\Delta\boldsymbol{\delta}$ from the nominal position to transition position, and then rotated $\Delta\boldsymbol{\theta}$ around point P_{rot} to actual position. The deflections of the reflection point P_{hit} due to the segment pose errors can be written as:

$$\Delta^0\boldsymbol{\delta} = {}^0_i\boldsymbol{T}\,\Delta^i\boldsymbol{\delta} \tag{6}$$

$${}^0\boldsymbol{s} = -{}^0_i\boldsymbol{T}({}^i\boldsymbol{p} - {}^i\boldsymbol{q})^{\times}\Delta^i\boldsymbol{\theta} \tag{7}$$

The incident-ray OPD produced by segments pose errors defined in LCS is

$$\Delta OPT = -\left(\frac{1}{{}^0\hat{\boldsymbol{i}}\cdot{}^0\hat{\boldsymbol{r}}}\right){}^0\hat{\boldsymbol{N}}^0_i\boldsymbol{T}\left[\Delta^i\boldsymbol{\delta} - \left({}^i\boldsymbol{p} - {}^i\boldsymbol{q}\right)^{\times}\Delta^i\boldsymbol{\theta}\right] \tag{8}$$

where ${}^0\circ$ is a vector defined in GCS $\{S_0\}$. ${}^i\circ$ is a vector defined in LCS $\{S_i\}$. $\hat{\boldsymbol{N}}$ is unit normal vector out of the nominal surface opposite to the incident-ray. $\vec{q}$ is the vector from PM vertex to the segment rotation point P_{rot}. $\vec{p}$ is the vector from PM vertex to the nominal reflection point P_{hit}. ${}^0_i\boldsymbol{T}$ is the transfer matrix from the GCS to the LCS. $\vec{v}^{\times}$ is the cross-product matrix operator of the vector $\vec{v}$. And

$$\vec{v}^{\times} = ([v_x, v_y, v_z]^T)^{\times} = \begin{bmatrix} 0 & -v_z & v_y \\ v_z & 0 & -v_x \\ -v_y & v_x & 0 \end{bmatrix}$$

The WD can be obtained by tracing all incident-rays using Eq. (8):

$$\Delta\boldsymbol{w} = \mathbf{A}\Delta\mathbf{X} \tag{9}$$

where $\Delta\boldsymbol{w} = \begin{bmatrix} \Delta OPT_1 \\ \Delta OPT_2 \\ \vdots \\ \Delta OPT_{mn} \end{bmatrix}$. $\Delta\mathbf{X} = \begin{bmatrix} \Delta^1\boldsymbol{\theta}_1 \\ \Delta^1\boldsymbol{\delta}_1 \\ \vdots \\ \Delta^m\boldsymbol{\theta}_m \\ \Delta^m\boldsymbol{\delta}_m \end{bmatrix}$.

$$\mathbf{A} = \begin{bmatrix} \partial L_1/\partial x_1 & \partial L_1/\partial x_2 & \cdots & \partial L_1/\partial x_{6m} \\ \partial L_2/\partial x_1 & \partial L_2/\partial x_2 & \cdots & \partial L_2/\partial x_{6m} \\ \vdots & \vdots & \ddots & \vdots \\ \partial L_{mn}/\partial x_1 & \partial L_{mn}/\partial x_2 & \cdots & \partial L_{mn}/\partial x_{6m} \end{bmatrix}.$$

where $x_{6i-5} = \Delta^i\theta_x; x_{6i-4} = \Delta^i\theta_y; x_{6i-3} = \Delta^i\theta_z; x_{6i-2} = \Delta^i\delta_x; x_{6i-1} = \Delta^i\delta_y; x_{6i} = \Delta^i\delta_z; i = 1 \sim m$

3.2. Wavefront deformation prediction

For definite segment pose errors, the accurate WD can be derived from Eq. (9). For the random segment pose errors, the accurate WD cannot be obtained, but their effects on the optical system can be evaluated by statistics. According to the discussion in Section 2, segments pose errors approximatively follow the multi-dimensional independent uniform distribution, and the expectation and variance of which can be obtained by Eq. (2). Set new random variables $\Delta\mathbf{X}'$, and

$$\Delta\mathbf{X}' = (\mathrm{diag}(\boldsymbol{\sigma}))^{-1}\Delta\mathbf{X} \tag{10}$$

where $\boldsymbol{\sigma}$ is the vector composed of the standard deviations of all segments pose errors.

Therefore $\Delta\mathbf{X}'$ is a vector consisting of independent random variables with the same distribution. And Eq. (9) can be expressed as:

$$\Delta\boldsymbol{w} = \mathbf{B}\Delta\mathbf{X}' \tag{11}$$

where $\mathbf{B} = \mathbf{A}\mathrm{diag}(\boldsymbol{\sigma})$.

The root mean square (RMS) is the most common and effective indicator for evaluating the WD. From Eqs. (2) and (9), the WD expectation is zero, so the mean square wavefront deformation (MSWD) can be written as:

$$RMS^2 = \frac{1}{mn}\Delta\boldsymbol{w}^T\Delta\boldsymbol{w} = \frac{1}{mn}\Delta\mathbf{X}'^T\mathbf{Q}\Delta\mathbf{X}' \tag{12}$$

where $\mathbf{Q} = \mathbf{B}^T\mathbf{B}$ is a symmetric matrix and can be decomposed as:

$$\mathbf{Q} = \mathbf{U}^T\boldsymbol{\Sigma}\mathbf{U} \tag{13}$$

where Σ is a diagonal matrix composed of the eigenvalue λ_l of $\mathbf{Q}$, and $\mathbf{U}$ is an orthogonal matrix consisting of the eigenvectors $\vec{v}_l$ of $\mathbf{Q}$.

Set $\Delta\mathbf{Y} = \mathbf{U}\Delta\mathbf{X}'$, and the MSWD can be written as:

$$RMS^2 = \frac{1}{mn}\Delta\mathbf{Y}^T\boldsymbol{\Sigma}\Delta\mathbf{Y} = \frac{1}{mn}\sum_{l=1}^{6m}\lambda_l\Delta\mathbf{Y}_l^2 \tag{14}$$

where $\Delta\mathbf{Y}$ is a vector composed of ΔY_l, and $\Delta Y_l = \vec{v}_l\Delta\mathbf{X}'$.

Since the variables $\Delta\mathbf{X}'$ are independent of each other, according to the central limit theorem (CLT), ΔY_l follow multidimensional independent normal distribution with a unit variance:

$$\Delta Y_l \sim \mathrm{N}(0,1) \tag{15}$$

ΔY_l^2 follows a chi-square distribution with one degree of freedom. The expectation and variance of MSWD are:

$$\begin{aligned} E(RMS^2) &= \tfrac{1}{mn}\textstyle\sum_{l=1}^{r}\lambda_l \\ D(RMS^2) &= \tfrac{2}{(mn)^2}\textstyle\sum_{l=1}^{r}\lambda_l^2 \end{aligned} \tag{16}$$

where r is the rank of $\mathbf{Q}$.

3.3. Numerical simulation

For the segmented PM described in Section 2, We trace 1037 uniformly distributed incident-rays on each segment surface, calculate the OPDs of all 1037 × m incident-rays reflected by the segmented PM, and obtain the total WD stemming from segments pose errors.

3.3.1. Simulations of segment pose error with definite value

For segments pose errors with definite value, the accurate WD can be obtained using Eq. (9). Taking the special cases (all segments pose errors are the same) for examples, the WDs are shown in Fig. 4. Fig. 4a to c are respectively the WDs with three DOFs $(\Delta\theta_x, \Delta\theta_y, \Delta\theta_z)$ attitude error $1''$ and Fig. 4d to f are respectively the WDs with three DOFs $(\Delta\delta_x, \Delta\delta_y, \Delta\delta_z)$ position error 1λ. It can be seen from Fig. 4 that each segment has the same WD in its own LCS, and the segmented PM has rotational symmetry wavefront aberration in GCS. This shows that Eq. (9) is effective, and it can calculate the WD produced by segments pose errors defined in LCS.

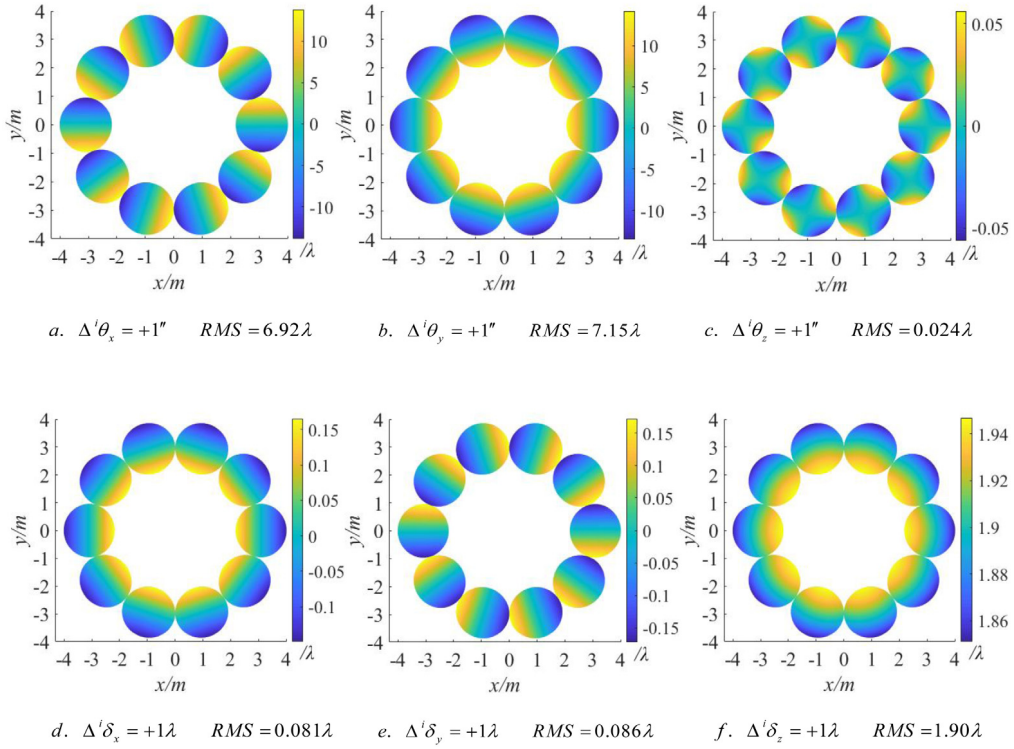

Fig. 4. The WD originating from single pose error with definite value.

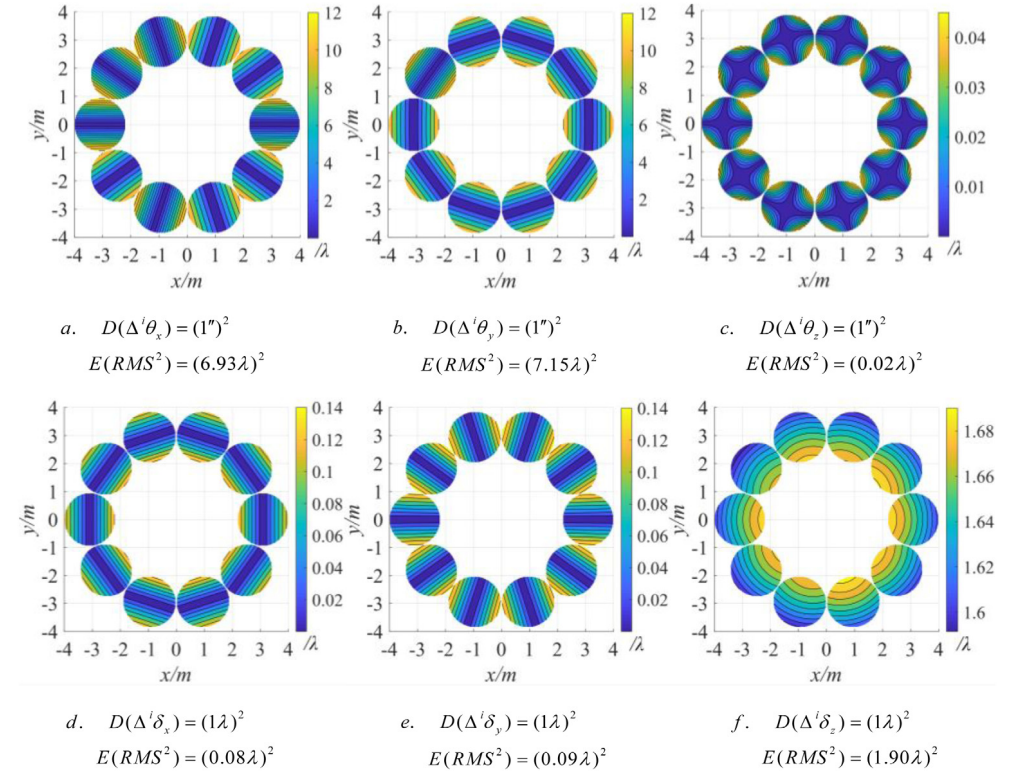

Fig. 5. The random WD originating from single random pose error.

It can also be seen from Fig. 4. The attitude error around the x-axis defined in the segment LCS produces a tip aberration in its own LCS, but all these segments aberrations manifest a high-order astigmatism on the system exit pupil. The attitude error around the y-axis defined in the segment LCS produces a tilt aberration in its own LCS, but all these segments aberrations manifest a high-order spherical aberration on the system exit pupil. The attitude error around the z-axis defined in the segment LCS produces an astigmatism aberration in its own LCS, but all these segments aberrations manifest a high frequency aberration on the system exit pupil. The position error along the x-axis defined in

the segment LCS produces a tilt aberration in its own LCS, but all these segments aberrations manifest a high-order spherical aberration on the system exit pupil. The position error along the y-axis defined in the segment LCS produces a tip aberration in its own LCS, but all these segments aberrations manifest a high-order astigmatism aberration on the system exit pupil. The position error along the z-axis defined in the segment LCS produces a defocus aberration in its own LCS, but all these segments aberrations manifest a high-order spherical aberration on the system exit pupil. Because of the randomness of the co-phasing errors, the probability of the system wavefront deformation manifesting a regular distribution is almost zero. The aberration produced by the random co-phasing errors presents approximate the influence of air turbulence, which contains few low-order aberrations.

3.3.2. Simulations of segment pose error with random value

Monte Carlo analysis which is referred as "the last method [27]" can address the uncertainty problem using statistics, hence it is very suitable for evaluating the WD originating from segment pose errors. According to Eq. (9), there are $6\times m$ random variables, which are the attitude errors $\Delta^i\boldsymbol{\theta}$ and position errors $\Delta^i\boldsymbol{\delta}$ of the segments from S_1 to S_m respectively. All of the variables follow the uniform distributions with the same expectation zero and different variances. By using software to generate the variable with the same distribution as the segment pose error, and simulating random sampling, the MSWD are:

$$RMS^2[\ RMS^2(\Delta\boldsymbol{w}_1)\ \cdots\ RMS^2(\Delta\boldsymbol{w}_{monte\_n})\ ] \tag{17}$$

where $\Delta\boldsymbol{w}_{monte\_n} = \mathbf{A}\Delta\mathbf{X}\mathrm{diag}(\boldsymbol{\varsigma}_{monte\_n})$. $\mathbf{A}$ is linear transfer matrix. $\boldsymbol{\varsigma}_{monte\_n}$ is the vector composed of the $monte_n$th random sampling variables. The larger the sampling quantity $monte\_n$, the closer the MSWD obtained by Eq. (17) is to the best expectation.

The WD stemming from the single DOF pose error is firstly presented to intuitively compare the effect of each segment pose error. The segmented PM model used in this simulations is the same as that described in Section 2. The expectation and variance of segment position errors are 0 and $(1\lambda)^2$ respectively and of segment attitude errors are 0 and $(1'')^2$ respectively. The mean of absolute value of all deformation maps is defined as the random WD map to avoid that positive OPD counteracts negative OPD, which can embody statistical law. The average WD maps are shown in Fig. 5, which indicate that in the LCS, segments random WD are approximately the same, while in the GCS, are still rotational symmetry. Comparing Figs. 4 and 5, it can be seen that the WD described in Fig. 4 is only a special case of the innumerable PM random WD. The effect of segments random pose errors is complex and cannot be described by an accurate WD, but its expectation and variance can be predicted through statistics, which can be used to evaluate its impact on the optical system. Moreover, the sensitivity of the WD to each DOF pose error is different, and the WD has the highest sensitivity to the x-axis, the y-axis rotation and the z-axis translation defined in LCS.

As discussion in Section 2, the segment positioning errors are accompanied in the whole phasing process, and the actual performance is the coupling of multiple pose errors (even if only one DOF phasing is performed), which is defined as mixed random pose errors. The analysis of the mixed random pose error is very complicated and not intuitive. But, the hybrid pose error can be decomposed into six random pose error components, the functions of which are equivalent. Using the same segmented PM model and the pose errors distributions, the random WD originating from the most complex pose error, including all six DOF pose perturbations, is shown in Fig. 6, which is an average deformation map accumulated by the absolute values of 10,000 random numerical simulation test results. Each numerical simulation result corresponds to a random set of six-degree-of-freedom co-phasing errors. Each set of co-phasing errors are randomly selected within the accuracy range according to the uniform distribution. For example, the position accuracy is $\pm\sqrt{3}\lambda$ and the attitude accuracy is $\pm\sqrt{3}''$, so the position errors take values within $[-\sqrt{3}\lambda, +\sqrt{3}\lambda]$, and the attitude errors take values within $[-\sqrt{3}'', +\sqrt{3}'']$ randomly.

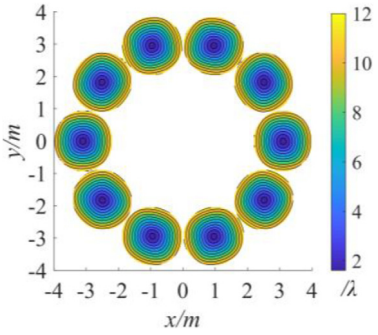

Fig. 6. The random WD originating from mixed random pose error ($E(RMS^2) = (10.14\lambda)^2$).

Because the 10,000 sets of co-phasing errors follow uniform distribution, the probability of segment co-phasing error along/round six degrees of freedom (DOF) is the same, and they are symmetric about the origin of the coordinate defined in the segment. The average WD map (Fig. 6) show a shape that is symmetric about the segment's origin, that is, an approximate defocusing effect. However, it is not defocus, because Fig. 6 is a superimposed map of statistics that does not really exist.

Moreover, it needs to be further explained that the average deformation map shown in Fig. 6 has an elliptical distribution (the fringes in the x-axis direction defined in the segment coordinate are slightly denser than that in y-axis) instead of a circular distribution, which is also correct. It can be seen from Fig. 4, the sensitivities of the WD to $\Delta^i\theta_x$, $\Delta^i\theta_y$ and $\Delta^i\delta_z$ are much greater than other co-phasing errors, the WDs produced by $\Delta^i\theta_y$ and $\Delta^i\delta_z$ are very similar, showing a tilt around the y-axis defined in the segment coordinate. Because the sum of the sensitivities of $\Delta^i\theta_y$ and $\Delta^i\delta_z$ is slightly greater than that of $\Delta^i\theta_x$, the fringes in the x-axis direction defined in the segment coordinate are slightly denser than that in y-axis. Fig. 6 also indicates that the more the pose error terms, the more complex the WD is, but the impact can still be evaluated by statistical laws.

3.3.3. Wavefront deformation prediction and its correction

In Section 3.2, the Eq. (16) for predicting the impact of segments random pose errors is derived. This section verifies its validity using Monte Carlo method. Using segmented PM models with different parameters, calculates the MSWD caused by pose errors with different bounds, and compares the results of Monte Carlo simulations with predictions. The PM aperture is 8 m with the paraxial ROC $R \in [8\ \mathrm{m}, 15\ \mathrm{m}]$, the conic constant $C_k \in [-2, 2]$, the segment quantity $m \in [2, 10]$, the segment diameter $r_{seg} \in [0.5\ \mathrm{m}, 0.95\ \mathrm{m}]$, the variance of segment position errors $D(\Delta^i\delta) \in [\ 0\ (100\lambda)^2\ ]$ and attitude errors $D(\Delta^i\theta) \in [\ 0\ (10'')^2\ ]$. Fig. 7 plots the verification results of 100 random sampling (the Monte Carlo sampling times of each sample is 10,000). The plots show that the formula has high prediction accuracy for MSWD expectation, but large deviation for variance. This is because the quantity of pose errors is so few that the WD produced by the errors only approximately follow normal distribution instead of strictly obey standard normal distribution, hence the conclusion of Eq. (14) is approximately instead of strictly established. In order to address this problem, the prediction formulas should be amended by the correction coefficients, and the revised formulas can be expressed as:

$$\begin{aligned} E(RMS^2) &= \frac{\zeta_E}{mn}\sum_{l=1}^{r}\lambda_l \\ D(RMS^2) &= \frac{2\zeta_D}{(mn)^2}\sum_{l=1}^{r}\lambda_l^2 \end{aligned} \tag{18}$$

where ζ_E is the expectation correction coefficient and ζ_D is the variance correction coefficient.

The expectations of correction coefficients are obtained by 1000 random samplings: $\zeta_E = 0.9997$ and $\zeta_D = 1/2.4710$. The prediction results after correction are shown in Fig. 8.

In order to comprehensively verify the prediction formulas, the numerical simulation conditions in Fig. 8 (including the paraxial ROC R, the conic constant C_k, the segment quantity m, the segment diameter r_{seg}, the co-phasing errors $\Delta^i\delta$ and $\Delta^i\theta$) are all randomly generated, and the ranges of conditions are the same as Fig. 7. That is why the distributions of the prediction $E(RMS^2)$ and simulation $E(RMS^2)$ in Figs. 7.a and 8.a are not the same. What is more, the max$D(RMS^2)$ in Fig. 7.b is 3.0e7 and that in Fig. 8.b is 1.2e7. They are on the same order of magnitude, which shows that the random validation method can approximately verify the prediction formula under extreme conditions, instead of simple data correction under the same conditions.

Because the $E(RMS^2)$ correction coefficient in Eq. (18) is approximately equal to 1 (0.9997), the max $E(RMS^2)s$ in Figs. 7.a and 8.a are close. And the $D(RMS^2)$ correction coefficient is smaller than 1 (1/2.4710), so the $D(RMS^2)$ in Fig. 8.b is smaller than that in Fig. 7.b.

At last, it can be seen from Fig. 8 that using the revised formula, the expectation prediction accuracy is difficult to be improved, remaining ±1%. However, the variance prediction accuracy is significantly improved to less than ±5%.

4. Weighted tolerance allocation of the pose errors

4.1. Diffraction-limited imaging conditions for optical system

According to the Marechal Criterion, the diffraction-limited imaging can be approximately obtained when the Strehl ratio of optical system is greater than 0.8. From the relationship between Strehl ratio and wavefront aberration:

$$\begin{aligned} Strehl\ ratio &= \frac{1}{\pi^2}\left|\int_0^{2\pi}\int_0^1 e^{i2\pi\Delta W(\rho,\theta)}\rho d\rho d\theta\right|^2 \\ &= 1-(2\pi\sigma)^2 \end{aligned} \tag{19}$$

Therefore, an optical system is regarded as diffraction-limited imaging when its WD σ is better than $\lambda/14$, which is the basis for system tolerance allocation. Because of the largest volume, complicated structure and numerous error sources, the segmented PM gets relatively relaxed tolerance $\lambda/23$, which needs to be further decomposed into PM polishing residual error, segments aspheric parameter errors and segments pose errors. According to the principle of identical tolerance, the pose-phasing error should be less than $\lambda/40$.

4.2. Weight coefficients construction for weighted tolerance allocation

The co-phasing platform is the most important device in the deployable optical system, and it is also the most expensive (mainly the technical difficulty of construction) device to be developed. Because the large-scale (centimeter-scale) nano-precision co-phasing platforms that meet the needs of space environments are difficult to achieve, even without regard to the construction cost and time. Take the most successful project, JWST, for example, the accuracy of its phasing platform can only meet the need of infrared imaging system, and for visible light imaging, the accuracy need to be increased by four times. So we need to use all possible methods to reduce the technical difficulty of construction. In other words, to develop reasonable indicators to make the phasing platform achievable using current technology.

The traditional co-phasing error allocation mostly bases on the principle of identical tolerance:

$$\Delta x_{tol\_i} = \sqrt{\frac{RMS_{total}^2}{n_p E(RMS_{tol\_i}^2)}} \tag{20}$$

where RMS_{total} is total tolerance. RMS_{tol_i} is the prediction of the WD RMS originating from each DOF segment pose error. n_p is the pose errors quantity of each segment.

The outstanding advantage of this allocation method is simple, but the disadvantages are obvious. It does not consider the sensitivity of the WD to different pose errors as well as the construction difficulties of disparate DOFs phasing precision, which result in some accuracy is difficult to achieve, but some is too easy. Taking the segmented PM introduced in Section 2 as an example, the allocation when the total tolerance is $\lambda/40(SR = 0.8)$ are $\theta x_{tol} = 1.47'' \times 10^{-3}(SR = 0.9959)$, $\theta x_{tol} = 1.47'' \times 10^{-3}(SR = 0.9959)$, $\theta z_{tol} = 0.51''(SR = 0.9959)$, $Tx_{tol} = 0.13\lambda(SR = 0.9959)$, $Ty_{tol} = 0.11\lambda(SR = 0.9959)$, $Tz_{tol} = 5.37 \times 10^{-3}\lambda(SR = 0.9959)$. The results of the allocation indicate that the difference between the highest precision and the lowest accuracy is three orders of magnitude, which is obviously unreasonable.

4.2.1. Constructing weight coefficients

In order to comprehensively evaluate the construction cost of the pose-phasing platform, the weight function $W_{tol\_i} = f(C_d, C_s)$ composed of the cost coefficient C_d and the sensitivity coefficient C_s is presented. The cost coefficient reflects the contribution of the linear actuators to segment pose errors, and the sensitivity coefficient represents the contribution of segment pose errors to the WD.

The coefficient C_s can be obtained from Eq. (18). The coefficient C_d is related to the structure of the pose-phasing mechanism. For the six DOFs parallel platform shown in Fig. 2, the transfer relationship between the actuator micro-displacement and the motion of the moving platform can be derived:

$$\Delta\mathbf{L} = \mathbf{P}\Delta\mathbf{X} \tag{21}$$

where $\Delta\mathbf{L}$ is the vector composed of the actuators positioning errors and $\mathbf{P}$ is the error transfer matrix.

When A is a full rank matrix, Eq. (20) is equivalent to

$$\Delta\mathbf{X} = \mathbf{P}^{-1}\Delta\mathbf{L} \tag{22}$$

The six DOFs rigid body motions of the parallel platform are completed by all linear actuators. The actuators have the highest utilization when the precision is the same, while the platform has the lowest construction cost. In this case, $\Delta\mathbf{L}$ is a vector consisting of random variables with the same distribution. The Monte Carlo method is used to predict the error transfer coefficient, which is the coefficient C_d representing the platform construction cost. The larger the C_d, the higher the platform construction cost, and, vice versa. Therefore, the pose error weight coefficient can be written as:

$$W_{tol\_i} = \frac{1}{C_d C_s} \tag{23}$$

4.2.2. Pose tolerance weighted allocation

The pose tolerance weighted allocation can be expressed as:

$$RMS_{tol\_i} = \frac{RMS_{total}}{W_{tol\_i}\sqrt{\sum_{tol\_i=1}^{n_p}\frac{1}{W_{tol\_i}^2}}} \tag{24}$$

where RMS_{tol_i} is the ith DOF segment pose tolerance and W_{tol_i} is the weight of RMS_{tol_i}.

Therefore, the tolerance allocation for the segmented PM described in Section 2 is $RMS_{\theta_x} = 1.47 \times 10^{-2}\lambda(SR = 0.9915)$, $RMS_{\theta_y} = 1.52 \times 10^{-2}\lambda(SR = 0.9909)$, $RMS_{\theta_z} = 4.01 \times 10^{-5}\lambda(SR = 1.0000)$, $RMS_{T_x} = 1.08 \times 10^{-3}\lambda(SR = 1.0000)$, $RMS_{T_y} = 1.21 \times 10^{-3}\lambda(SR = 0.9999)$, $RMS_{T_z} = 1.31 \times 10^{-2}\lambda(SR = 0.9932)$. It can be seen from the results that this allocation sufficiently balances the effects of the sensitive and insensitive errors. For the sensitive errors such as $RMS_{\theta x}$, $RMS_{\theta y}$ and RMS_{Tz}, relatively larger tolerances are assigned, and for the insensitive errors such as $RMS_{\theta z}$, RMS_{Tx} and RMS_{Ty}, smaller tolerances are assigned. The linear actuators precision tolerances ΔL_{tol} corresponding to the tolerance allocation can be obtained using Eq. (21), and are all equal to 20.38 nm, which indicates that the construction cost of each actuator is the same.

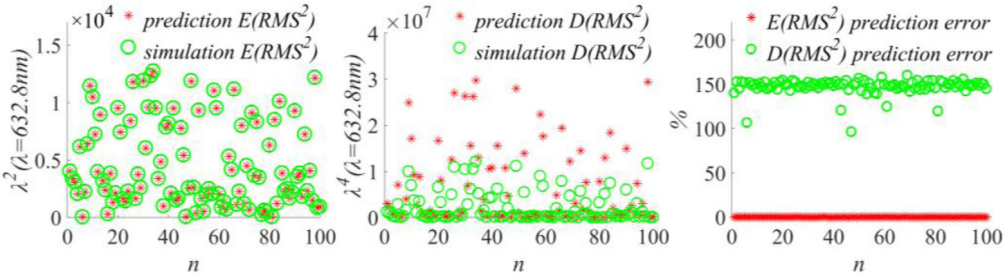

a. RMS^2 expectation prediction b. RMS^2 variance prediction c. Prediction errors

Fig. 7. Verification results of 100 random sampling for WD originating from different pose errors of segmented PMs with disparate parameter (before correction).

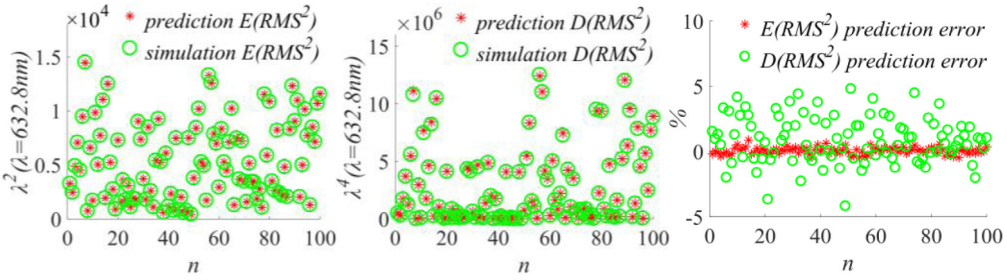

a. RMS^2 expectation prediction b. RMS^2 variance prediction c. Prediction errors

Fig. 8. Verification results of 100 random sampling for WD originating from different pose errors of segmented PMs with disparate parameter (after correction).

Table 1
The pose-phasing platform positioning precision.

T_x nm	T_y nm	T_z nm	θ_x nrad	θ_y nrad	θ_z nrad
11.79	11.80	6.07	14.30	14.30	13.48

4.2.3. Numerical simulation

The numerical simulation is achieved to calculate the positioning errors of the pose-phasing platform as the linear actuator precision is 20.38 nm (Table 1).

Fig. 9 is the probability distribution of the WD stemming from the positioning errors shown in Table 1. where its ordinate is the probability density. As can be seen from the plot, the WD RMS approximately follows the normal distribution, and the expectation and standard deviation are 0.020λ and 0.0017λ respectively. This indicates that the WD RMS is less than 0.0251λ at the 99.87% confidence probability, which is perfectly consistent with the input 0.025λ, and verifies that the weighted tolerance allocation method can reasonable assign the pose tolerance under the condition of the lowest technical difficulty of construction.

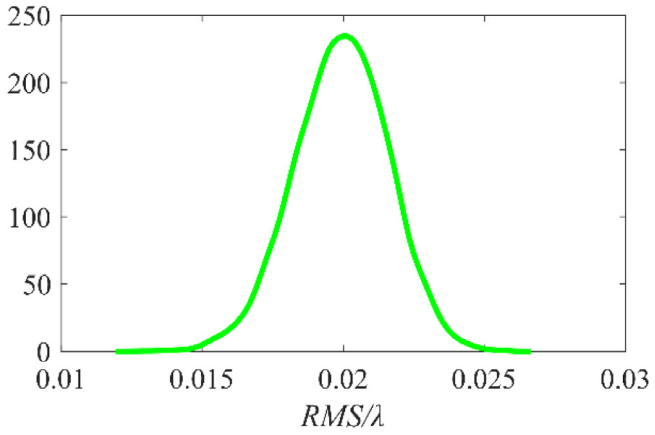

Fig. 9. The probability distribution of the WD stemming from the positioning errors shown in Table 1.

5. Conclusion

This paper deduces the linear sensitivity matrix of the wavefront deformation to segments pose errors defined in local coordinate system, derives the prediction formula of the wavefront deformation stemming from segments random pose errors, and proposes the method of weighted tolerance allocation to control the pose-phasing platform construction cost. The numerical simulations indicate that random pose errors will generate uncertain wavefront deformation, which can be effectively predicted by the formula presented in this paper. The prediction errors of the expectation are less than ±1% and the prediction errors of the variance are less than ±5%. It is significant to allocate tolerances reasonably, which can effectively control the platform construction cost, and the technical difficulty of construction can be minimized using the allocation method introduced in this paper.

Acknowledgments

The authors thank Baixu Liu and Xi Chen for providing good suggestions. This work was supported by the National Key Technologies R&D Program of China (Grant No. 2016YFB0500100).

References

[1] J.M. Oschmann, M. Clampin, H. MacEwen, Special section guest editorial: Space telescopes, Opt. Eng. 52 (9) (2013) 091801.
[2] J.S. Fender, Future trends in large space optics, Proc. SPIE 4013 (2000) 682–686.
[3] N. Rioux, H. Thronson, L. Feinberg, H.P. Stahl, D. Redding, A. Jones, J. Sturm, C. Collins, A. Liu, A future large-aperture UVOIR space observatory: reference designs, Proc. SPIE 9602 (2015) 960205.
[4] D.C. Redding, L. Feinberg, M. Postman, H.P. Stahl, C. Stahle, H. Thronson, Beyond JWST: Performance requirements for a future large UVOIR space telescope, Proc. SPIE 9143 (2014) 914312.
[5] C.F. Lillie, Large deployable telescopes for future space observatories, Proc. SPIE 5899 (2005) 58990D.

[6] H.P. Stahl, H. Thronson, S. Langhoff, M. Postman, D. Lester, C.F. Lillie, R.J. Brissenden, Potential astrophysics science missions enabled by NASA's planned Ares V, Proc. SPIE 7436 (2009) 743607.
[7] H.S. Yang, X.J. Zhang, Z.L. Li, H. Bao, Y.C. Fan, Technology and development of deployable segmented ultra-large-aperture space remote sensors, Opt. Precis. Eng 26 (6) (2018) 1287–1298.
[8] C. Atkinson, S. Texter, R. Keski-Kuha, L. Feinberg, Status of the JWST optical telescope element, Proc. SPIE 9904 (2016) 990403.
[9] M. Postman, T. Brown, K. Sembach, M. Giavalisco, W. Traub, K. Stapelfeldt, D. Calzetti, W. Oegerle, R.M. Rich, H.P. Stahl, J. Tumlinson, M. Mountain, R. Soummer, T. Hyde, Advanced technology large-aperture space telescope: science drivers and technology developments, Opt. Eng. 51 (1) (2012) 011007.
[10] J.J. Rey, A. Wirth, A. Jankevics, F. Landers, D. Rohweller, C.B. Chen, A. Bronowicki, A deployable, annular, 30 m telescope, space-based observatory, Proc. SPIE 9143 (2014) 914318.
[11] A. Jacob, P. Parihar, A co-phasing technique for segmented mirror telescopes, Proc. SPIE 9654 (2015) 96540G.
[12] D. Yue, S.Y. Xu, H.T. Nie, Co-phasing of the segmented mirror and image retrieval based on phase diversity using a modified algorithm, Appl. Opt. 54 (26) (2015) 7917–7924.
[13] H. Choi, I. Trumper, M. Dubin, W.C. Zhao, D.W. Kim, Simultaneous multi-segmented mirror orientation test system using a digital aperture based on sheared fourier analysis, Opt. Express 25 (15) (2017) 18152–18164.
[14] Z. Liao, Q. Qui, H. Xian, Self-calibrating phase measurement based on diffraction theory and numerical simulation experiments, Opt. Eng. 54 (2) (2015) 025116.
[15] K.N. Yao, J.L. Wang, X.Y. Liu, H.W. Li, M.H. Wang, B.C. Cui, S.H. Yu, Pyramid wavefront sensor using a sequential operation method, Appl. Opt. 54 (13) (2015) 3894–3901.
[16] J.L. Jiang, W.R. Zhao, Phasing piston error in segmented telescopes, Opt. Express 24 (17) (2016) 19123–19137.
[17] J.F. Simar, Y. Stockman, J. Surdej, Single-wavelength coarse phasing in segmented telescopes, Appl. Opt. 54 (5) (2015) 1118–1123.
[18] G.H. Ju, C.X. Yan, Z.Y. Gu, Elimination of the field-dependent aberrations of the JWST-like space telescopes in the multi-field fine-phasing process, Appl. Opt. 56 (10) (2017) 2724–2740.
[19] G. Chanan, M. Troy, Strehl ratio and modulation transfer function for segmented mirror telescopes as functions of segment phase error, Appl. Opt. 38 (31) (1999) 6642–6647.
[20] J.L. Flores, M. Strojnik, G. Páez, García-Torales G, Effects of misalignment error on the optical transfer functions of synthetic aperture telescopes, Appl. Opt. 43 (32) (2004) 5926–5932.
[21] J. Zhang, W.R. Zhao, F. Yang, L.F. Zhang, The effects of piston error on image quality of synthetical aperture optical imaging system, Proc. SPIE 8557 (2012) 85570Z.
[22] Z. Liu, S.Q. Wang, L.H. Huang, C.H. Rao, Analysis of Relationship Between Far-field Images and Piston Error of Synthetic-aperture Telescopes for the Broadband Target Wave, Proc.IEEE- 2010 OSA-IEEE-cos Advences in Optoelectronics and Micro/Nano-Optics, 2011, pp. 1-5.
[23] H.S. Yang, X.J. Zhang, Z.L. Li, X.K. Wang, M.M. Xu, Study of the impact of co-phasing errors for segmented primary mirror using nonlinear analysis, Optik - Int. J. Light Electron Opt. 191 (2019) 80–88.
[24] J. Ding, Research on Methodologies for Accuracy Analysis and Synthesis of Six-Dof Parallel Mechanism (Doctoral dissertation), Harbin Institute of Technology, 2015.
[25] Z.H. Yi, Development of Motion Simulation and Accuracy Prediction System of Parallel Platform with Six Degrees of Freedom (Doctoral dissertation), Harbin Institute of Technology, 2014.
[26] D.C. Redding, W.G. Breckenridge, Optical modeling for dynamics and control analysis, J. Guid. Control Dyn. 14 (1991) 1021–1032.
[27] C.L. Kang, The Theory and Application of Monte Carlo Method, Science Press, Beijing, 2015.